Aerospace Science and Technology 139 (2023) 108383

Contents lists available at ScienceDirect

Aerospace Science and Technology

journal homepage: www.elsevier.com/locate/aescte

Numerical studies of flow patterns and fuel distribution of tandem-arranged multi jets in a hypersonic crossflow

Jialin Wang [a,b], Guilai Han [a,b,*]

[a] State Key Laboratory of High Temperature Gas Dynamics, Institute of Mechanics, Chinese Academy of Sciences, 100190 Beijing, China
[b] School of Engineering Sciences, University of Chinese Academy of Sciences, 100049 Beijing, China

ARTICLE INFO

Article history:
Received 26 October 2022
Received in revised form 16 March 2023
Accepted 7 May 2023
Available online 12 May 2023
Communicated by Yu Lv

Keywords:
Hypersonic flow
Tandem-arranged jets
Streamline pattern
Vortex structure
Fuel-air mixing

ABSTRACT

In this study, the numerical analysis of the three-dimensional flow fields of a series of tandem-arranged equal-strength hydrogen jets injected into a Mach 8 hypersonic crossflow is presented. The study comparatively analyzes the flow field similarities and differences between different configurations, namely, single, double, and quadruple jets. The results indicate that downstream jets do not have a significant effect on the first Mach cell and only slightly lift the bow shock at downstream compared with the single jet case. Additionally, high-temperature regions in all cases are in close proximity to the hydrogen stoichiometric equivalence ratio interface, making the fuel more prone to pre-ignition. Moreover, flow patterns in inter-gap regions and vortex structures are compared casewise. In addition, hydrogen injected from each orifice is traced, and the mass fraction distribution contributed by each jet on the symmetry plane and the inter-gap region is analyzed to derive the mixing characteristics.

1. Introduction

Oblique detonation engines (ODEs) do not have to carry oxidizer and have a high combustion efficiency and heat release rate due to the characteristics of the oblique detonation wave (ODW), granting them a great prospect of application in hypersonic vehicle engines [1,2]. Recent years have seen much progress in the research on detonation wave mechanisms and detonation engine characteristics. However, a common assumption in the existing studies is the mixed fuel-air inflow condition, especially in ODW or ODE modeling and numerical simulations [3–6]. However, the successful establishment of the ODW at the inlet of the combustor demands a high degree of fuel-air mixing conditions [7–9]. If these conditions are not satisfied, the ODE might fail to work. Therefore, seeking an efficient and feasible fuel-air mixing method for the actual ODEs has become an urgent task.

Two significant problems exist in the mixing process of ODEs: achieving a high penetration depth and a sufficient mixing process and avoiding pre-ignition at the inlet. The first problem stems from the high Mach number in the ODE inlet. As detonation is premixed combustion, the fuel must be injected at the inlet instead of the combustor in scramjets. Since the operating Mach number of ODEs is in the range of 6-22 [10], the freestream at the inlet is still hypersonic even though slowed down by the compressing oblique shock at the lip of the inlet, which could inhibit fuel penetration and dispersion [11,12]. Intrusive mixing devices [13], such as the cantilevered ramp, are widely used in scramjet combustors. However, the severe aerodynamic heating brought by the hypersonic crossflow can erode the geometry of such intrusive devices and thereby diminish their vortex generation ability, namely the mixing efficiency. The increasing complexity of the cooling system is also not beneficial for hypersonic vehicles [14]. Additionally, the wave drag and high total pressure loss can also reduce ODE performance [15]. Therefore, the common fuel injection scheme does not apply to ODEs.

Since the detonation is premixed combustion, pre-ignition should be avoided as much as possible because it does affect ODW establishment and stabilization. However, in Veraar and Mayer's experimental investigation [16], where a wall-mounted hydrogen jet was injected into the Mach 3.25 crossflow with the stagnation temperature of 1450 K, pre-ignition still existed in the boundary layer separation zone

* Corresponding author.
E-mail address: hanguilai@imech.ac.cn (G. Han).

https://doi.org/10.1016/j.ast.2023.108383
1270-9638/

and the flow field outside of the boundary layer despite of the relative low incoming Mach number. Gamba and Mungal [17] draw a similar conclusion by experimentally investigating the transverse hydrogen jet in a Mach 2.4 supersonic crossflow with a total temperature of 3000 K. Through OH planar laser-induced fluorescence imaging, they found that at a higher jet-to-crossflow momentum flux ratio J, the reaction region is in the near wall region and the shear layer. Therefore, compared with intrusive mixing devices, the wall-mounted injection method is more likely to pre-combust in the boundary layer and downstream of the bow shock as the high stagnation temperature brought by the intrusive mixing devises is not blocked.

Based on the pros and cons of intrusive structures and wall-mounted injectors, a combination of these two methods has led to the design of the aerodynamic ramp. The aerodynamic ramp proposed by Cox et al. [14] was constituted of nine injectors arranged in a 3×3 matrix. The transverse angles of the three rows of injectors were 15°, 30°, and 45° designed to generate vortical interactions and enhance mixing. Such an arrangement could utilize the injector spacings, yaw angle, injector transverse angles, and dynamic pressure ratios to enhance the mixing process [18,19]. Fuller et al. [20] experimentally demonstrated that in a Mach 2 crossflow, the 3×3 aerodynamic ramp had less total pressure loss and better mixing performance in the near-field compared with the physical ramp. Although the physical ramp has better far-field mixing under lower momentum flux ratios, the mixing performance of the aerodynamic ramp could be compensated by a higher J. Despite the demonstrated advantages of applying the aerodynamic ramp as a probable solution for the fuel injection method of ODEs, there still lacks a principal guidance to direct the injection scheme design.

The aerodynamic ramp could be regarded as a set of multiple injectors that could be optimized in terms of injector positions, mass flow rates or momentum flux ratios, and injection angles [21]. To simplify the problem, multiple injectors could be represented by tandem- and parallel-arranged multijet. Further, the parallel-arranged multijet could be simplified into a single jet with periodic boundary conditions in simulation. Considering the complex interaction between the adjacent jet and the synergistic effect induced by the upstream jets, the tandem-arranged multijet is a more suitable model for multiple jets. Lee [22,23] investigated the characteristics of two equal-strength jets in supersonic crossflow, including the basic flow structures, vortex structures, interaction between two jets, and how the burning of upstream injections affects the flow field structures. The optimum spacing based on the penetration depth is related to the momentum rate of each jet. However, the definite relationship between spacing, penetration depth, and momentum rate still requires further study.

Characteristics of single jets [24–26], pulsed jets, staged, and double jets [27–29] were comparatively investigated numerically and experimentally which provide basic physical insights into the jet supersonic crossflow interaction flow field. Multiple jets and micro-jets were also used to diminish the fraction and enhance the mixing process, significantly improving the mixing process compared to the baseline cases [30]. Although various fuel delivery strategies have shown promising characteristics in mixing enhancement, the theoretical mixing mechanism has not been fully understood and thoroughly revealed [21]. Therefore, the mechanism of the tandem-arranged multijet as a basic model still needs to be ascertained.

To reveal the mixing enhancement mechanism of multi-jet in the hypersonic crossflow, three-dimensional flowfields of the tandem-arranged multijet with different configurations, i.e., single, double, and quadruple jets, injected into the Mach 8 hypersonic crossflow were comparatively analyzed in this study. In Sec 2, numerical methods and computational setup were introduced. Numerical validation and grid resolution analysis were presented in Sec 3. Results and discussions, including flow structures associated with the interaction patterns, vortex structures, temperature distribution, fuel mass fraction distribution and construction were detailed in Sec 4. Finally, conclusions were presented in Sec 5.

2. Numerical details

2.1. Physical and mathematical models

Three-dimensional compressible Navier-Stokes (N-S) equations combined with the two-equation shear stress transport (SST) turbulence model [31] and multi-component non-reaction model in the integrated form are used to simulate the hypersonic transverse jet interaction:

$$\frac{\partial Q}{\partial t} + \frac{\partial}{\partial x}(F_1 - G_1) + \frac{\partial}{\partial y}(F_2 - G_2) + \frac{\partial}{\partial z}(F_3 - G_3) = \dot{S} \tag{1}$$

Q is the dependent variable vector; F_1, F_2, and F_3 are the inviscid flux vector components; G_1, G_2, and G_3 are the viscous flux vector components; and $\dot{S}$ is the source term vector. These are calculated as follows:

$$Q = \begin{bmatrix} \rho \\ \rho u \\ \rho v \\ \rho w \\ \rho e \\ \rho k \\ \rho \omega \\ \rho Y_1 \\ \vdots \\ \rho Y_{ns-1} \end{bmatrix} F_1 = \begin{bmatrix} \rho u \\ \rho u^2 + p \\ \rho uv \\ \rho uw \\ (\rho e + p)u \\ \rho uk \\ \rho u\omega \\ \rho uY_1 \\ \vdots \\ \rho uY_{ns-1} \end{bmatrix}_1 F_2 = \begin{bmatrix} \rho v \\ \rho uv \\ \rho v^2 + p \\ \rho vw \\ (\rho e + p)v \\ \rho vk \\ \rho v\omega \\ \rho vY_1 \\ \vdots \\ \rho vY_{ns-1} \end{bmatrix} F_3 = \begin{bmatrix} \rho w \\ \rho uw \\ \rho vw \\ \rho w^2 + p \\ (\rho e + p)w \\ \rho wk \\ \rho w\omega \\ \rho wY_1 \\ \vdots \\ \rho wY_{ns-1} \end{bmatrix} \dot{S} = \begin{bmatrix} 0 \\ 0 \\ 0 \\ 0 \\ 0 \\ S_k \\ S_\omega \\ 0 \\ \vdots \\ 0 \end{bmatrix}$$

$$G_1 = \begin{bmatrix} 0 \\ \tau_{xx} \\ \tau_{xy} \\ \tau_{xz} \\ u\tau_{xx} + v\tau_{xy} + w\tau_{xz} + q_x \\ (\mu_l + \sigma_k\mu_t)\frac{\partial k}{\partial x} \\ (\mu_l + \sigma_\omega\mu_t)\frac{\partial \omega}{\partial x} \\ \rho\,(D_l + D_t)\frac{\partial Y_1}{\partial x} \\ \vdots \\ \rho\,(D_l + D_t)\frac{\partial Y_{ns-1}}{\partial x} \end{bmatrix} G_2 = \begin{bmatrix} 0 \\ \tau_{yx} \\ \tau_{yy} \\ \tau_{yz} \\ u\tau_{yx} + v\tau_{yy} + w\tau_{yz} + q_y \\ (\mu_l + \sigma_k\mu_t)\frac{\partial k}{\partial y} \\ (\mu_l + \sigma_\omega\mu_t)\frac{\partial \omega}{\partial y} \\ \rho\,(D_l + D_t)\frac{\partial Y_1}{\partial y} \\ \vdots \\ \rho\,(D_l + D_t)\frac{\partial Y_{ns-1}}{\partial y} \end{bmatrix} G_3 = \begin{bmatrix} 0 \\ \tau_{zx} \\ \tau_{zy} \\ \tau_{zz} \\ u\tau_{zx} + v\tau_{zy} + w\tau_{zz} + q_z \\ (\mu_l + \sigma_k\mu_t)\frac{\partial k}{\partial z} \\ (\mu_l + \sigma_\omega\mu_t)\frac{\partial \omega}{\partial z} \\ \rho\,(D_l + D_t)\frac{\partial Y_1}{\partial z} \\ \vdots \\ \rho\,(D_l + D_t)\frac{\partial Y_{ns-1}}{\partial z} \end{bmatrix} \tag{2}$$

where $\rho, p, u, v, w, k, \omega$ are density, pressure, velocity components in the x, y, and z directions, the turbulent kinetic energy, and the specific dissipation rate; Y_i is the mass fraction of component i; ns is the number of the component; e is the total internal energy of mixed gas per unit mass, and

$$e = h - \frac{p}{\rho} + \frac{1}{2}\left(u^2 + v^2 + w^2\right) + k \tag{3}$$

where h is the total enthalpy per unit mass. The stresses and strains are as follows:

$$\begin{aligned}
\tau_{xx} &= 2(\mu_l + \mu_t)\frac{\partial u}{\partial x} - \frac{2}{3}(\mu_l + \mu_t)\vartheta - \frac{2}{3}\rho k \\
\tau_{yy} &= 2(\mu_l + \mu_t)\frac{\partial v}{\partial y} - \frac{2}{3}(\mu_l + \mu_t)\vartheta - \frac{2}{3}\rho k \\
\tau_{zz} &= 2(\mu_l + \mu_t)\frac{\partial w}{\partial z} - \frac{2}{3}(\mu_l + \mu_t)\vartheta - \frac{2}{3}\rho k \\
\tau_{xy} &= \tau_{yx} = (\mu_l + \mu_t)\left(\frac{\partial u}{\partial y} + \frac{\partial v}{\partial x}\right) \\
\tau_{xz} &= \tau_{zx} = (\mu_l + \mu_t)\left(\frac{\partial u}{\partial z} + \frac{\partial w}{\partial x}\right) \\
\tau_{yz} &= \tau_{zy} = (\mu_l + \mu_t)\left(\frac{\partial w}{\partial y} + \frac{\partial v}{\partial z}\right)
\end{aligned} \tag{4}$$

where μ_l and μ_t are the laminar viscosity and the turbulent viscosity of the mixture. ϑ is the dilatation, which can be expressed as follows:

$$\vartheta = \frac{\partial u}{\partial x} + \frac{\partial v}{\partial y} + \frac{\partial w}{\partial z} \tag{5}$$

Heat transfer rates are as follows:

$$\begin{aligned}
q_x &= -(\kappa_l + \kappa_t)\cdot\frac{\partial T}{\partial x} - \sum_{i=1}^{ns}\rho\,(D_l + D_t)\,h_i\frac{\partial Y_i}{\partial x} \\
q_y &= -(\kappa_l + \kappa_t)\cdot\frac{\partial T}{\partial y} - \sum_{i=1}^{ns}\rho\,(D_l + D_t)\,h_i\frac{\partial Y_i}{\partial y} \\
q_z &= -(\kappa_l + \kappa_t)\cdot\frac{\partial T}{\partial z} - \sum_{i=1}^{ns}\rho\,(D_l + D_t)\,h_i\frac{\partial Y_i}{\partial z}
\end{aligned} \tag{6}$$

where κ_l and κ_t are the laminar and turbulent heat transfer coefficients of the mixture, and D_l and D_t are the laminar and turbulent diffusion coefficients of the mixture. In this study, the N-S equations are solved using the finite volume method. The Harten-Lax van Leer contact (HLLC) approximate Riemann scheme [32] with the min-mod limiter [33] is used to compute the second-order convective flux F_i. The viscous flux G_i is computed using a simple second-order average of all vertex polynomials. Time advancement is performed by implicit backward Euler integration with multi-grid acceleration and dual time-stepping methods [34].

2.2. Computational details

To investigate the flow pattern and the mixing mechanism of tandem-arranged jets in a hypersonic flow field, this study conducted three cases, namely, a single transverse jet as the baseline, tandem-arranged double jets, and tandem-arranged quadruple jets. Sonic jets are used and hydrogen is injected transversely. In all three cases, the jet diameter $d_j = 2$ mm, $Ma_j = 1$, $p_{0j} = 0.5$ MPa, $T_{oj} = 300K$. The ODE is expected to be operated at an altitude of 30 km, and therefore the atmospheric condition at 30 km is adopted with the freestream static pressure $p_\infty = 1197$ Pa and static temperature $T_\infty = 226.5$ K. A Mach 8 crossflow is used to simulate the hypersonic flow condition

Table 1
Inflow and jet conditions.

Inflow	Jet
$Ma_\infty = 8$	$Ma_j = 1$
$p_\infty = 1197$ Pa	$p_{0j} = 0.5$ MPa
$T_\infty = 226.5$ K	$T_{0j} = 300$ K
$Re_\infty = 2.96\times\ 10^6$ /m	$J = 3.45$

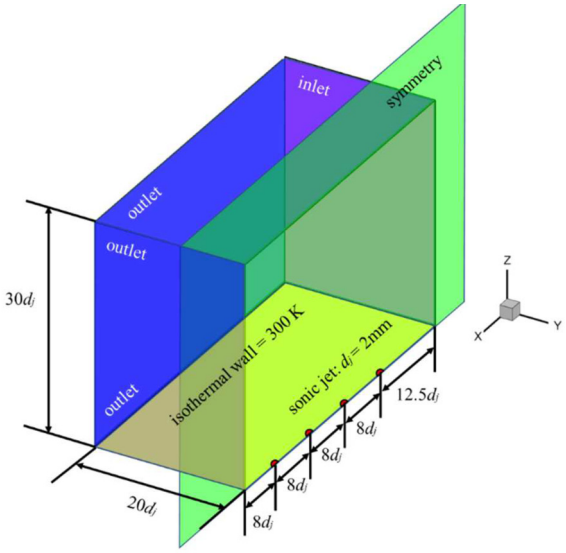

Fig. 1. Schematic of the computational domain and boundary conditions in the tandem-arranged quadruple jets case.

Table 2
Inflow and jet conditions in previous experiments [35].

Inflow	Air jet
$Ma_\infty = 1.6$	$Ma_j = 1$
$p_{0\infty} = 241$ KPa	$p_{0j} = 0.48$ MPa
$T_{0\infty} = 295K$	$T_{0j} = 295$ K
$Re_\infty = 58.8\times\ 10^6$ /m	$J = 1.7$

at the inlet of the ODE. The corresponding jet momentum ratio $J = \frac{\gamma_j p_j Ma_j^2}{\gamma_\infty p_\infty Ma_\infty^2} = 3.45$ and the unit Reynold number is $Re_\infty = 2.96\times\ 10^6$ /m. Flow conditions used in this paper are listed in Table 1.

The schematic of the computational domain and boundary conditions of tandem-arranged quadruple jets are shown in Fig. 1. To save computational resources, only half model is computed by using the symmetry plane in $y = 0$, and the boundary layer solution at 0.08 m from the leading edge solved by the numerical method described in Sec 2 with the incoming flow condition in Table 1 is assigned to the inflow boundary condition. In all three cases, the origin is set at the center of the most upstream jet and 0.105 m from the leading edge of the flat plate. Therefore, the inflow boundary condition is 0.025 m ($12.5dj$) upstream of the first jet, which could completely contain the separation region before the first jet. In tandem-arranged jet cases, the interval between the two jets L is $8dj$, which could well capture the recirculation flow pattern in the gap. An isothermal wall condition is adopted and set as 300 K. The computational domain extends in the spanwise direction from $y = 0dj$ to $y = 20dj$ and in the wall-normal direction from $z = 0dj$ to $z = 30dj$, which could completely contain the general flowfield structures. Supersonic outflow conditions are set at the slice of $z = 30dj$, $y = 20dj$, and $x = 32dj$.

3. Validation and grid resolution analysis

To validate the computational method, velocity and pressure distributions in the experiment of Santiago and Dutton [35] are used for comparison against the numerical solution obtained using the numerical methods in this paper. In their experiment, a sonic air jet with $d_j = 4$ mm was injected transversely into the Mach 1.6 supersonic crossflow, and the boundary layer thickness at $x/d_j = -5$ is $\delta_{99} = 0.775d_j$. Flow conditions in Santiago and Dutton's experiments are listed in Table 2.

In the validation, the computational domain size is designed according to the wind tunnel's test section with 36 mm high and 72 mm wide. The total element is 2.6 million with the first layer spacing of mesh is 2.5e-5 m. In addition to the experimental data, numerical results in [36,37] based on LES and ILES turbulent models are also used for comparison in this paper. Fig. 2 demonstrates the streamwise velocity profiles solved in this paper using the SST turbulent model and the comparison with experimental data in [35], Kawai and Lele's LES numerical results [36], and Rana et al.'s ILES numerical results [37] at $x/d_j = -1.5$, 2, 3, 4, 5. Despite the discrepancies between all numerical results and the experimental data, the flow feature capturing capacities of the three numerical methods appear consistent. Fig. 3 shows the pressure distribution on $z/d_j = 0$, 1, 2 and the comparison with experimental data in [35], Kawai and Lele's LES numerical results [36], and Rana et al.'s ILES numerical results. In Fig. 3(a) the differences between numerical results and experimental data in the

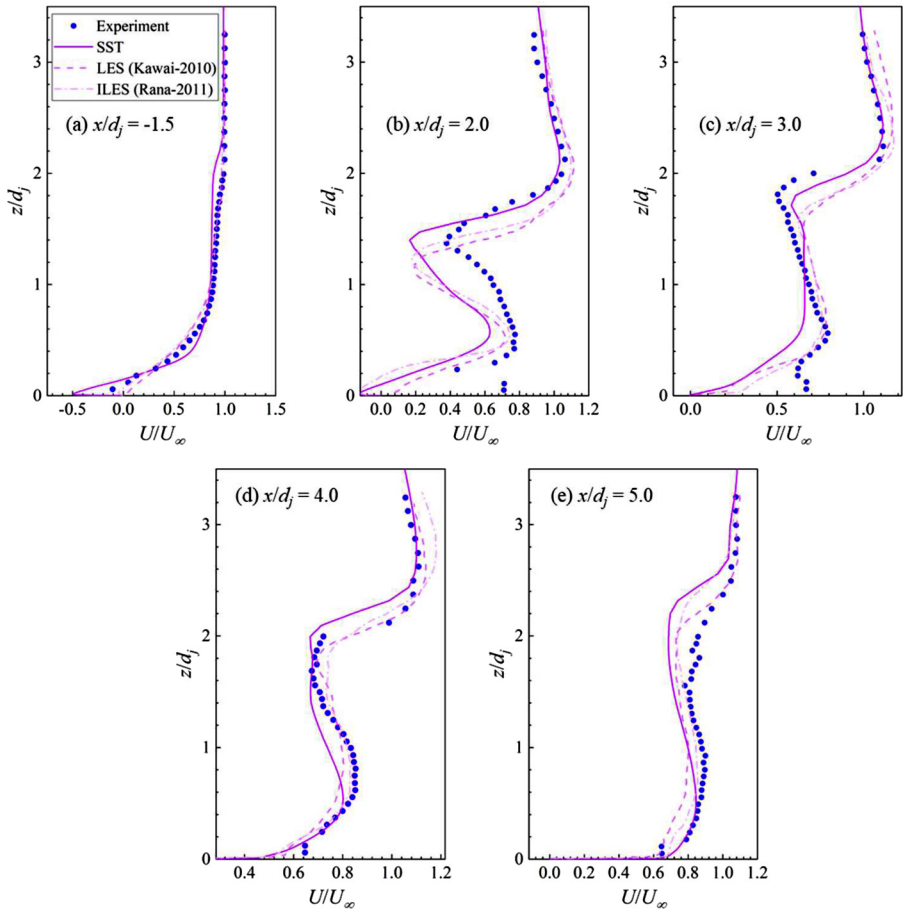

Fig. 2. Comparisons of streamwise velocity profiles at $x/d_j = -1.5$, 2, 3, 4, and 5 in experiments [35] (blue dot) and numerical results of the numerical methods in this paper with the SST turbulent model (solid line), Kawai and Lele's numerical results with the LES turbulent model [36] (dashed line), and Rana et al.'s numerical results with the ILES turbulent model [37] (dash-dot line). (For interpretation of the colors in the figure(s), the reader is referred to the web version of this article.)

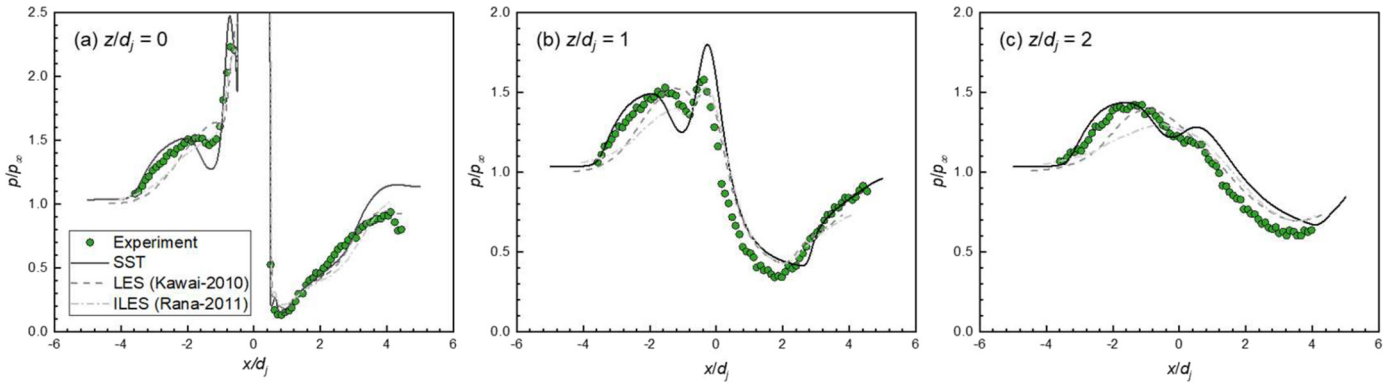

Fig. 3. Comparisons of pressure distributions at $z/d_j = 0$, 1, 2 in experiments [35] (green dot) and numerical results of the numerical methods in this paper with the SST turbulent model (solid line), Kawai and Lele's numerical results with the LES turbulent model [36] (dashed line), and Rana et al.'s numerical results with the ILES turbulent model [37] (dash-dot line).

upstream separation region may be caused by the high unsteadiness [37,38] of the jet in supersonic crossflow; the pressure distribution in the downstream recirculation region agrees with the predictions of the numerical results. From the distribution of the pressure data curves, it can be seen that the numerical method used in this study can accurately capture the pressure distribution at different spanwise positions and agrees relatively well with the numerical results of Kawai (LES) and Lele and Rana et al. (ILES). Based on the above comparisons, it can be concluded that the numerical methods used in this paper are appropriate for subsequent investigations.

The tandem-arranged double jets with the geometry in Fig. 1 and the initial condition listed in Table 1 in three meshes with different resolutions are used to verify grid independence. The height of the first grid Δs in the wall-normal direction (z direction), the corresponding z^+, the number of nodes in the three directions (n_x, n_y, and n_z), and the total elements in each mesh are listed in Table 3. Details of the medium grid in tandem-arranged double jets are demonstrated in Fig. 4. Both structured and unstructured grids are used on the wall. Nodes are clustered around the jet exit and set uniformly in the gap between the two jets. In the wake region, the nodes gradually

Table 3
Parameters of three different meshes.

Mesh	Δs/m	z^+	n_x	n_y	n_z	Total elements
coarse	5.0e-5	< 5.0	440	70	120	10.64e+6
medium	1.0e-6	< 1.0	652	100	276	21.28e+6
fine	1.0e-6	< 1.0	800	150	276	37.11e+6

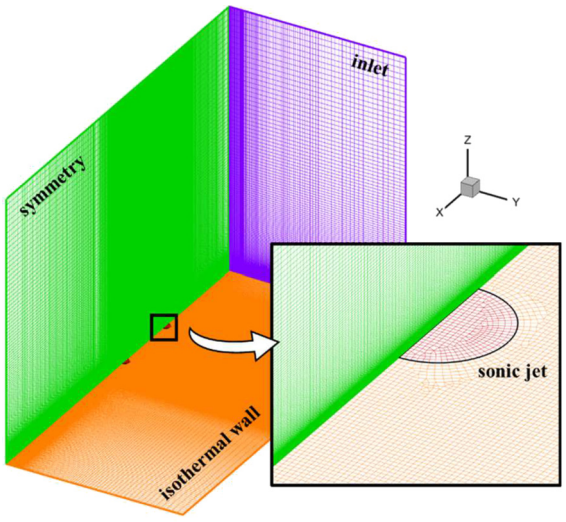

Fig. 4. Grid construction details of double jets: full-size figure of grids and the zoomed-in figure of grid arrangement around jet orifice and near-wall region.

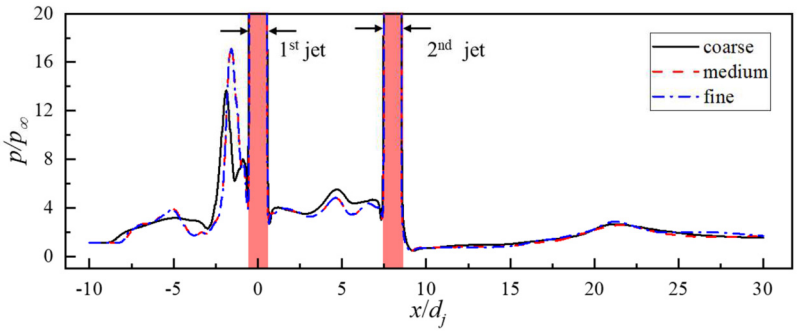

Fig. 5. Pressure distributions on the wall of symmetry plane predicted by coarse grid (black solid line), medium grid (red dashed line), and fine grid (blue dot-dash line). Regions through jet orifices are colored red.

become sparse to the outlet to reduce the total elements. Elements in the outer flow region are generated by extruding the wall grid in the wall-normal direction.

The non-dimensional wall pressure distribution on the wall of the symmetry plane derived from different meshes is shown in Fig. 5. The pressure distribution solved by medium and fine grids coincides well with each other, including the pressure rise at the boundary layer separation position, the pressure fluctuation in the separation region caused by the horseshoe vortex, the pressure distribution in the downstream recirculation region, and the pressure rise generated by the reflect shock-boundary layer interaction. Compared with medium and fine grids, the pressure distribution in the gap of the two jets predicted by the coarse grid is slightly higher, and the separation length is longer. In conclusion, to save computational resources, the medium grid is adopted in the subsequent computation.

4. Results and discussions

4.1. General flowfield structures

The main structures of flowfields in single, double, and quadruple jets are shown in Fig. 6 using the density gradient magnitude contour on the symmetry plane, including the separation shock, bow shock, jet shear layer, Mach cell, and Mach disk. The second jet in double and quadruple-jet cases has a complete Mach cell structure under $L/d_j = 8$. Moreover, in multi-jet cases, the structure of the upper-most jet is not affected by downstream jets as the Mach cell of the upper-most jet in the two cases is nearly the same. Additionally, bow shock shapes in the three cases have nearly the same curvature according to the shock positions in the three cases extracted and compared in Fig. 7. Discrepancies between the three shocks and a slight lift brought by the increasing downstream jets only appeared after $12d_j$. Although the downstream jets do not affect the upstream structure in this paper, it can be speculated that with the increasing of J or the decreasing of the gap, the Mach cell of the downstream jet might interact with the upstream Mach cell and affect the bow shock

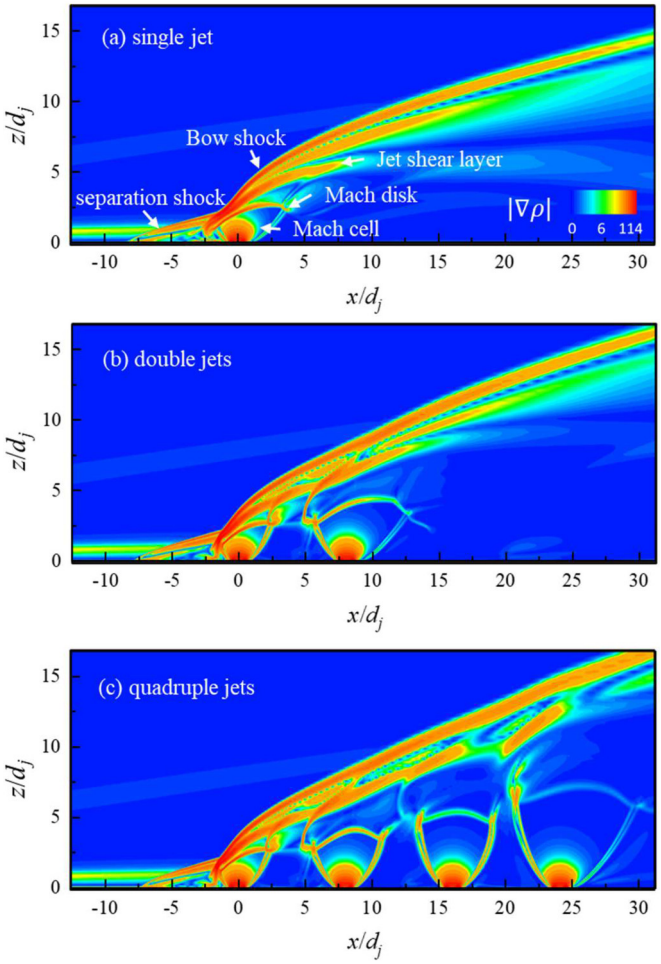

Fig. 6. Flow structures in (a) single, (b) double, and (c) quadruple jets cases represented by $|\nabla\rho|$ on the symmetry plane.

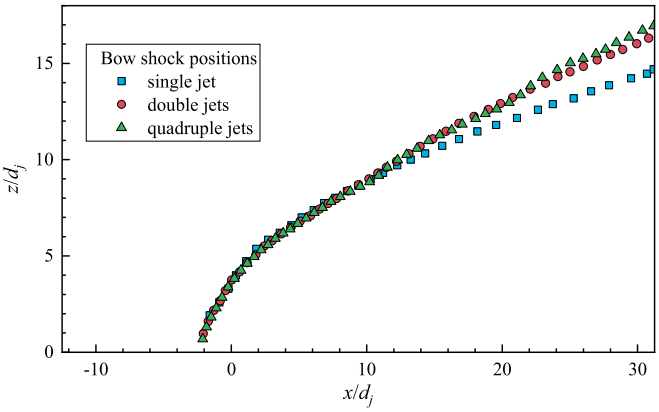

Fig. 7. Bow shock positions on the symmetry plane in single, double, and quadruple-jet cases.

structure. Also, disturbance generated by downstream jets might spread upstream through the subsonic region, mostly underneath each Mach cell. Mach contour on the symmetry plane in the quadruple-jet case is shown in Fig. 8.

4.2. Streamline patterns and vortex structures

In tandem-arranged jets, flow interactions between two jets can promote the fuel-air mixing process. Therefore, the streamline patterns and vortex structures are thoroughly analyzed to reveal the effect of the inter-hole recirculation region in promoting the mixing process.

To visualize the flow patterns, the non-dimensional pressure distribution on the symmetry plane and wall overlapped with two-dimensional streamlines are presented in Figs. 9 to 11. Streamline patterns of the single transverse jet are relatively simple, dominated by two recirculation regions denoted as R1 and R2 in the upstream separation region, another recirculation region in the leeward of the Mach cell, and the wake region elongated into the far downstream. In addition to the high-pressure region behind the bow shock, another

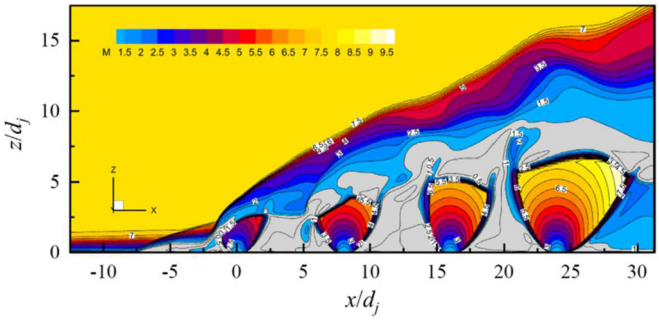

Fig. 8. Mach contour on the symmetry plane in the quadruple-jet case.

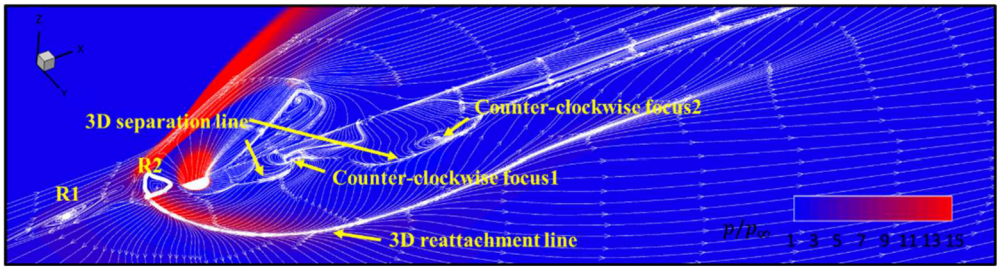

Fig. 9. Non-dimensional pressure distribution on the symmetry and wall plane covered by two-dimensional streamlines in the single jet case.

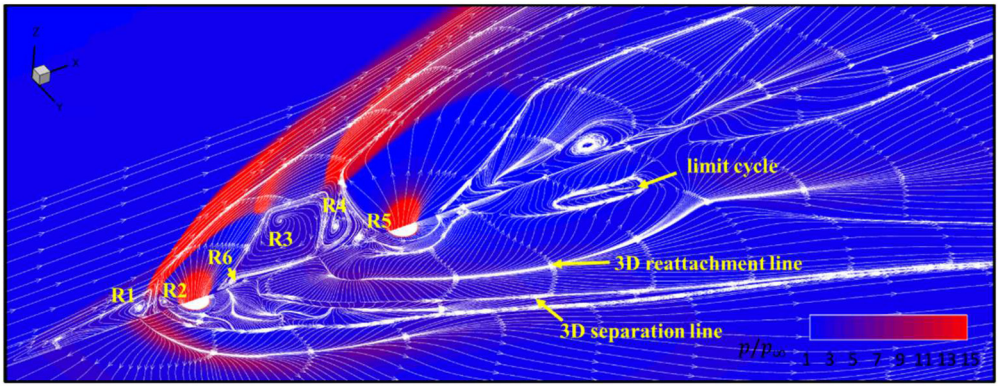

Fig. 10. Non-dimensional pressure distribution on the symmetry and wall plane covered by two-dimensional streamlines in the case of double jets.

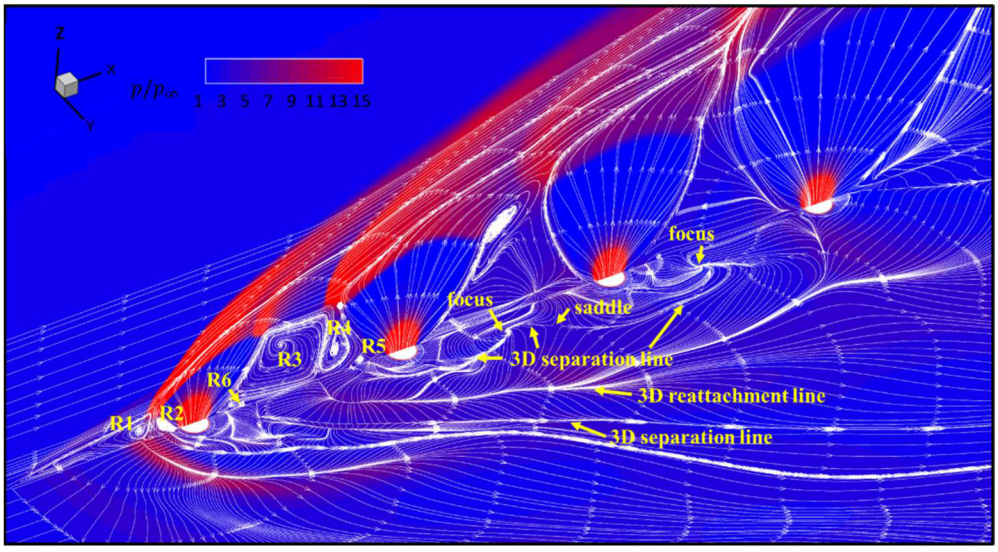

Fig. 11. Non-dimensional pressure distribution on the symmetry and wall plane covered by two-dimensional streamlines in quadruple-jet case.

high-temperature region on the wall is along the reattachment line in the separation region, which is generated by the fluid impingement between the two recirculation regions. Saddles and nodes on the wall are generated by the three-dimensional flow interactions. In the case of a single transverse jet, two obvious counter-clockwise focuses can be seen in Fig. 9. As shown in Fig. 9, the three-dimensional separation line behind the Mach cell on the wall spiraling into the counter-clockwise focus 1 indicates fluid rolling up from the wall into the outer flow. This separation is caused by the adverse pressure gradient in the leeward of the Mach cell. Further downstream, another three-dimensional separation line spiraling into the counter-clockwise focus 2 is generated by the interaction between two streams of fluid. One stream is derived from R2, and the other is from the side rim. These two streams wrapped around the Mach cell with different spinning directions meet downstream and interact.

In the case of double jets, four recirculation regions denoted as R3 to R6 appear in the gap. Among them, R5 and R6 are in the corner flow and the secondary recirculation region. Though these two recirculation regions have complex near-wall interactions indicated by the streamline topology, they cannot affect the macro fluid structure. Flows in R4 bend around the second jet and then interact and mix with the wake of the second jet, which is demonstrated by the large stable limit cycle on the wall. Flows in R3 bend around the second jet too, but then stretch sideways and turn downstream, which is presented by the separation and reattachment lines on the wall.

In the case of quadruple jets, streamline patterns before the second jet are the same as in the double-jet case, i.e., four recirculation regions in the first gap. However, only one recirculation region close to the second jet's Mach disk is shown in the second gap, and no recirculation region is shown in the third. The reason is the less interaction between the outer high-speed jet plum and the low-speed fluid in the inter-gap region. Blocked by the upstream Mach cell, the downstream under-expanded jet could expand in an environment with a lower crossflow Mach number and static pressure. As a result, the lower local momentum ratio leads to a large Mach cell and high penetration depth, making the fluid direction through the Mach disk closer to vertical so that it interacts less with the inter-gap fluid. In terms of fluid interactions, fluid in R3 stretch sideways, as in the double-jet case. Fluid in R4 wraps around the second jet and interacts with the inter-gap fluid in the second and third gaps, as demonstrated by the focus-saddle-focus combination topology with a three-dimensional separation line linking each critical point.

As streamlines cannot reflect the vortex structure well [39], the third-generation vortex identification method Liutex [40–43] is used for vortex identification, which is accomplished by using code LiutexUTA released by Chaoqun Liu at the University of Texas at Arlington. Liutex has been extensively verified and compared with other vortex identification methods [44–46] and used in compressible [47] and incompressible flows [48,49], where it demonstrated great advantages.

Liutex is defined as a vector $\vec{R} = R\vec{r}$. R represents the rotation intensity of the fluid element along the local rotation axis. $\vec{r} = r_x i + r_y j + r_z k$ represents the direction of the local rotation axis of the fluid element in the origin reference frame. The Liutex criterion first finds a reference frame where the fluid element has rotational motion only in a plane orthogonal to the local Z-axis. Then, the motion of the fluid element is decomposed to analyze whether there is rigid rotation along the Z-axis. Finally, the value of the Liutex vector is defined as twice the rigid body rotational angular velocity of the fluid parcel along the Z-axis and can be calculated as follows:

$$R_z = 2\omega_{rot} = \begin{cases} 2(\beta - \alpha), & \text{if} \alpha^2 - \beta^2 < 0, \beta > 0 \\ 2(\beta + \alpha), & \text{if} \alpha^2 - \beta^2 < 0, \beta < 0 \\ 0, & \text{if} \alpha^2 - \beta^2 \geq 0 \end{cases} \tag{7}$$

$$\begin{aligned} \alpha &= \frac{1}{2}\sqrt{\left(\frac{\partial V}{\partial Y} - \frac{\partial U}{\partial X}\right)^2 + \left(\frac{\partial V}{\partial X} + \frac{\partial U}{\partial Y}\right)^2} \\ \beta &= \frac{1}{2}\left(\frac{\partial V}{\partial X} - \frac{\partial U}{\partial Y}\right) \end{aligned} \tag{8}$$

Where XYZ is the local reference frame of the fluid particle and U, V, W are velocity components of the fluid particle in the local reference frame. Since the Liutex vector is derived by decomposing the motion of fluid elements and coordinate transformation, without involving the compressibility of the fluid, it is applicable to both compressible and incompressible flow fields. Compared with the Q criterion, the Liutex criterion is less susceptible to shear contamination in compressible flow fields. Additionally, Liutex is a vector while Q is a scalar, making the Liutex criterion more intuitive for analyzing the direction of vortex rotation.

To understand these flow fields more comprehensively, vortex structures from the bottom view and the corresponding wall streamlines are presented in Figs. 12 to 14. Vortex structures generated by different jets and gaps are colored according to the streamwise position to distinguish among them, as visualized by Liutex iso-surface with Liutex magnitude $|R| = 200000$. For the single transverse jet, apart from horse-shoe vortexes in the separation region, three apparent trailing vortexes elongate downstream. According to the wall streamline, these vortexes are confined in a narrow gap close to the symmetry plane.

Upon the appearance of the second jet, the three trailing vortex structures in the single jet case disappear, and two strong vortex structures appear in the gap, corresponding to R3 and R4 in Fig. 11. As the vortex in R4 elongates around the second jet, another vortex stretches into the spanwise direction behind the large stable limit cycle, which is generated by baroclinic effect brought by the reflection shock-boundary layer interaction. This out-stretched vortex divides the wake region behind the second jet into two parts, each containing one trailing vortex. Additionally, the trailing vortex behind the out-stretched vortex is wider than that in the single jet case thanks to the larger Mach cell of the second jet.

Though more complex vortexes appear in the quadruple-jet case, the vortex structures are the least developed among the three cases due to the shrinking space of the downstream inter-region. Therefore, to improve the mixing efficiency, the spacing between the downstream gaps can be appropriately increased for the porous and equal-strength serial jet. Otherwise, under the constant spacing between jets, the strength of the downstream jet could be reduced.

4.3. High-temperature region and fuel distribution

To ensure the successful detonation wave establishment at the inlet of combustion in ODEs, premature fuel combustion should be avoided as much as possible. Therefore, the high-temperature region in the flow field should be reduced. The high-temperature region

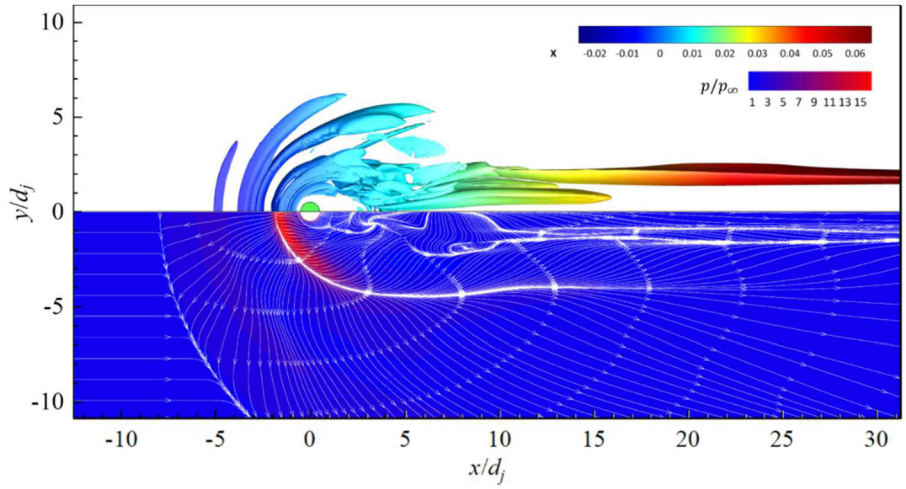

Fig. 12. Vortex structures of the single jet case in the bottom view visualized by Liutex with $|R| = 200000$ with the corresponding wall streamline overlapped on the non-dimensional wall pressure distribution.

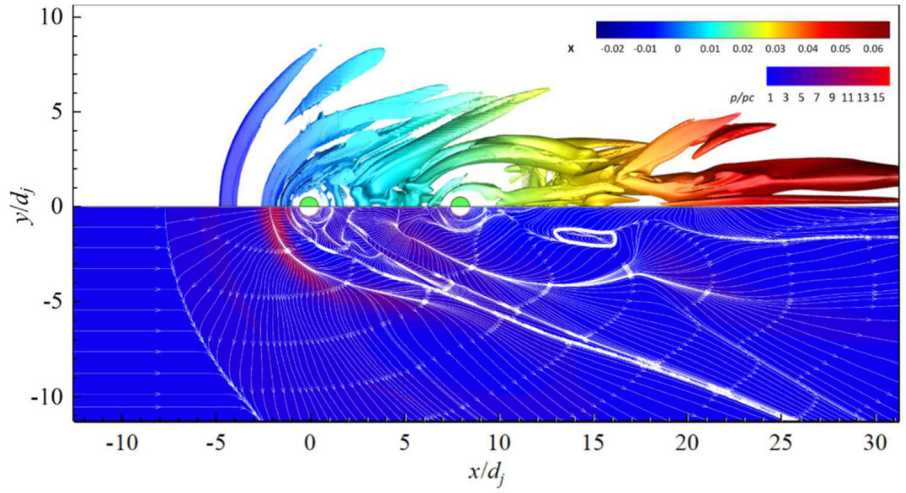

Fig. 13. Vortex structures of the double-jet case in the bottom view visualized by Liutex with $|R| = 200000$ with the corresponding wall streamline overlapped on the non-dimensional wall pressure distribution.

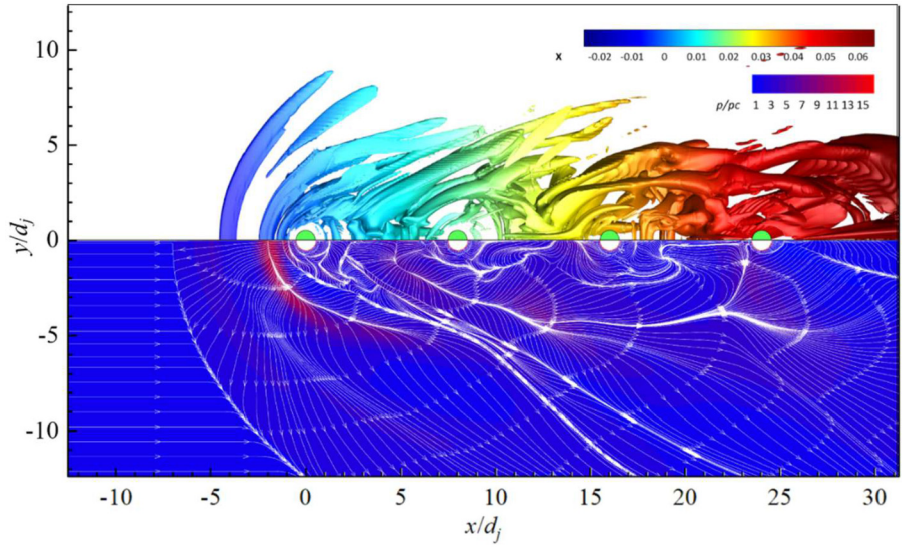

Fig. 14. Vortex structures of the quadruple-jet case in the bottom view visualized by Liutex method with $|R| = 200000$ combined with corresponding wall streamline overlapped on the non-dimensional wall pressure distribution.

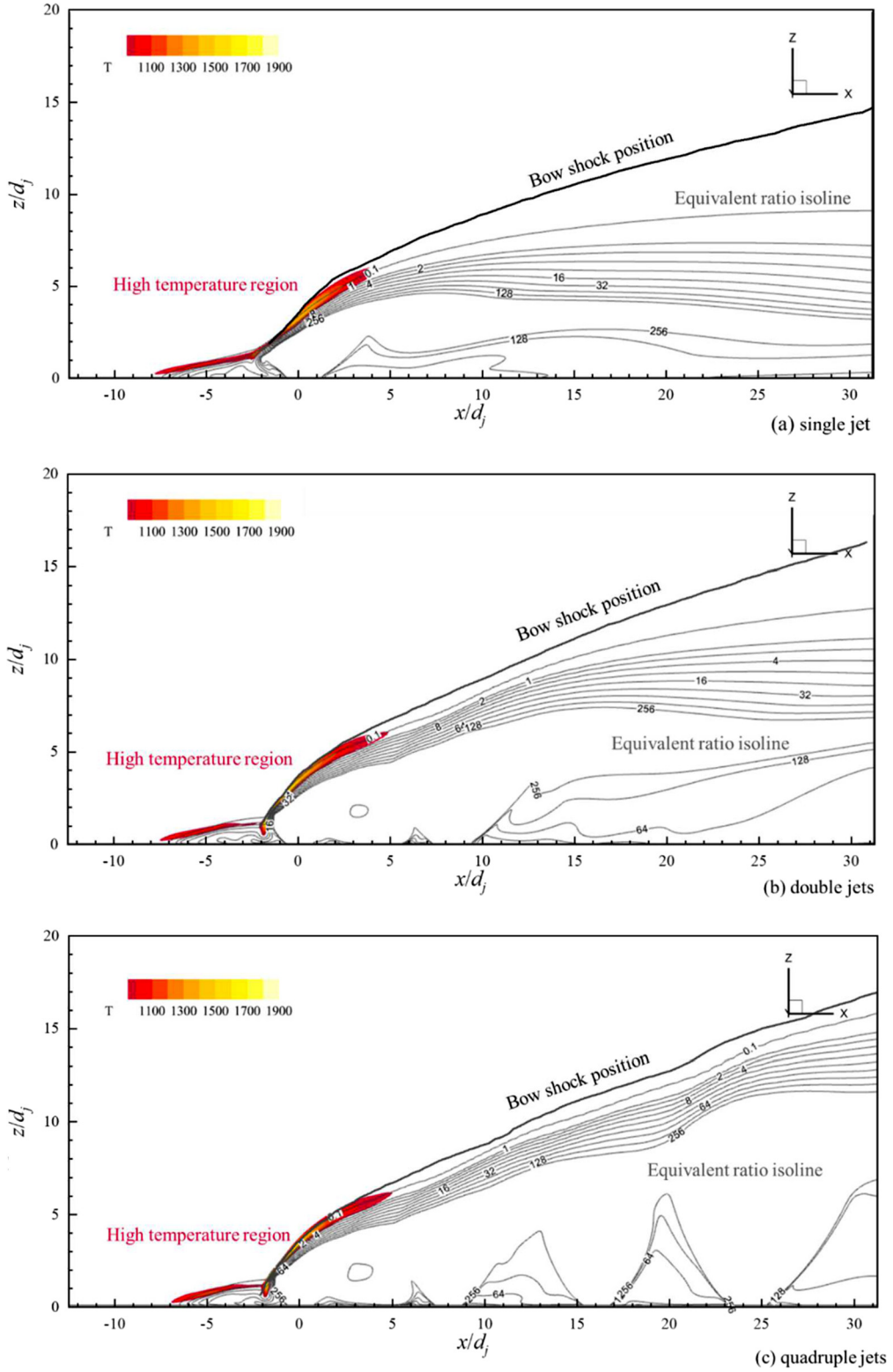

Fig. 15. High-temperature region above 900 K and hydrogen equivalent ratio isolines on the symmetry in (a) single, (b) double, and (c) quadruple-jet cases.

above 900 K and the hydrogen equivalent ratio (ER) isolines on the symmetry plane of the single, double, and quadruple-jet cases are shown in Fig. 15. According to the high-temperature region distribution, it is mainly generated by the separation shock and the bow shock also close to the interface of ER=1. Thus, advanced combustion may occur in the high-temperature region.

To further analyze the fuel concentration distribution in the flow field and the contribution of each jet, the distribution of hydrogen ejected from each jet is presented in Fig. 16 and Fig. 17 through component tracking. In both double and quadruple-jet cases, hydrogen ejected from the most upstream jet can be completely distributed in all regions behind the bow shock except the downstream Mach

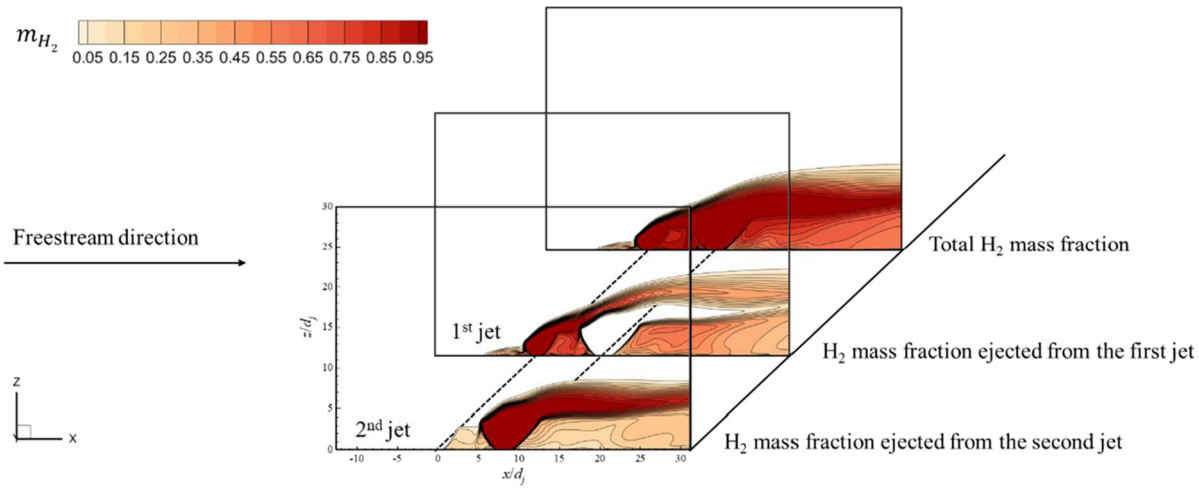

Fig. 16. Hydrogen mass fraction distribution generated by each jet in double jets case.

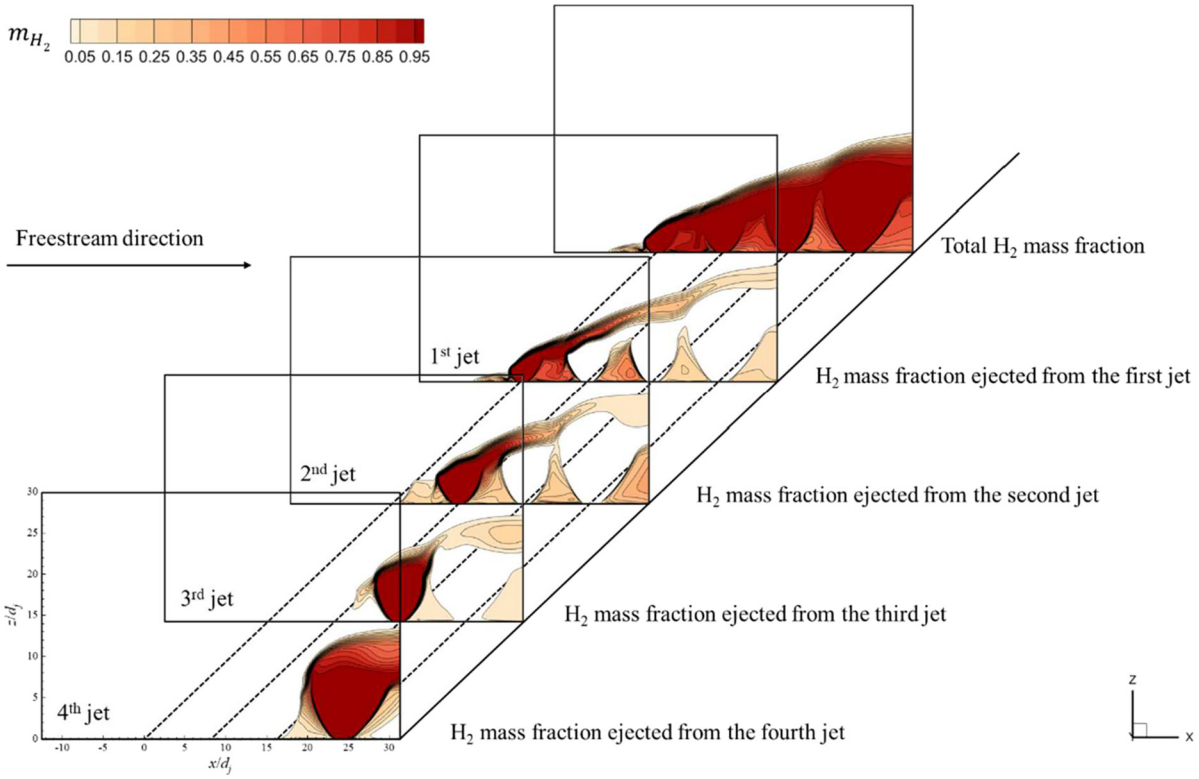

Fig. 17. Hydrogen mass fraction distribution generated by each jet in quadruple jets case.

cell. Moreover, fuel ejected from the downstream jet can, at most, be transferred to the upstream inter-gap region between the two jets. Likewise, it can also cover the whole area after the downstream bow shock except the downstream Mach cell.

To quantitatively assess the contribution of each jet at the critical inter-region, we extract three vertical lines in each gap on the symmetry plane. In each line, the total mass fraction of hydrogen and that contributed by each jet in the quadruple-jet case are compared and demonstrated in Fig. 18.

In lines $x = 2d_j$ and $4d_j$, the hydrogen mass fraction distribution is dominated by the injection from the first jet. The injection from the second jet only concentrates in the lower half of the whole hydrogen plum and contributes a little fraction. The overlapped region in Fig. 18 demonstrates the mixing between different jets, where the hydrogen from the first and second jets in lines $x = 2d_j$ and $4d_j$ mix with each other comprehensively. As lines $x = 6d_j$ and $10d_j$ pierce through the second jet's Mach cell, hydrogen from the second jet dominates the center part of the construction of the whole plum. Nevertheless, injection from the first jet still dominates the upper and lower parts of the whole hydrogen plum. In the second gap, from the outer region into the wall, line $x = 12d_j$ goes through the plums of the first and second jets. It is worth noticing that, though the plum of the second jet contributes most of the mass fraction, hydrogen from the first jet still dominates the lower half of the whole jet plum. Lines $x = 14d_j$ and $18d_j$ pierce through the third jet's Mach cell, and the mass fraction contributed by the first and second jets show a double-peak distribution along the two lines. In the upper half of $x = 14d_j$, injection from the second jet contributes more than the first. In the near wall region, the first jet contributes twofold more than

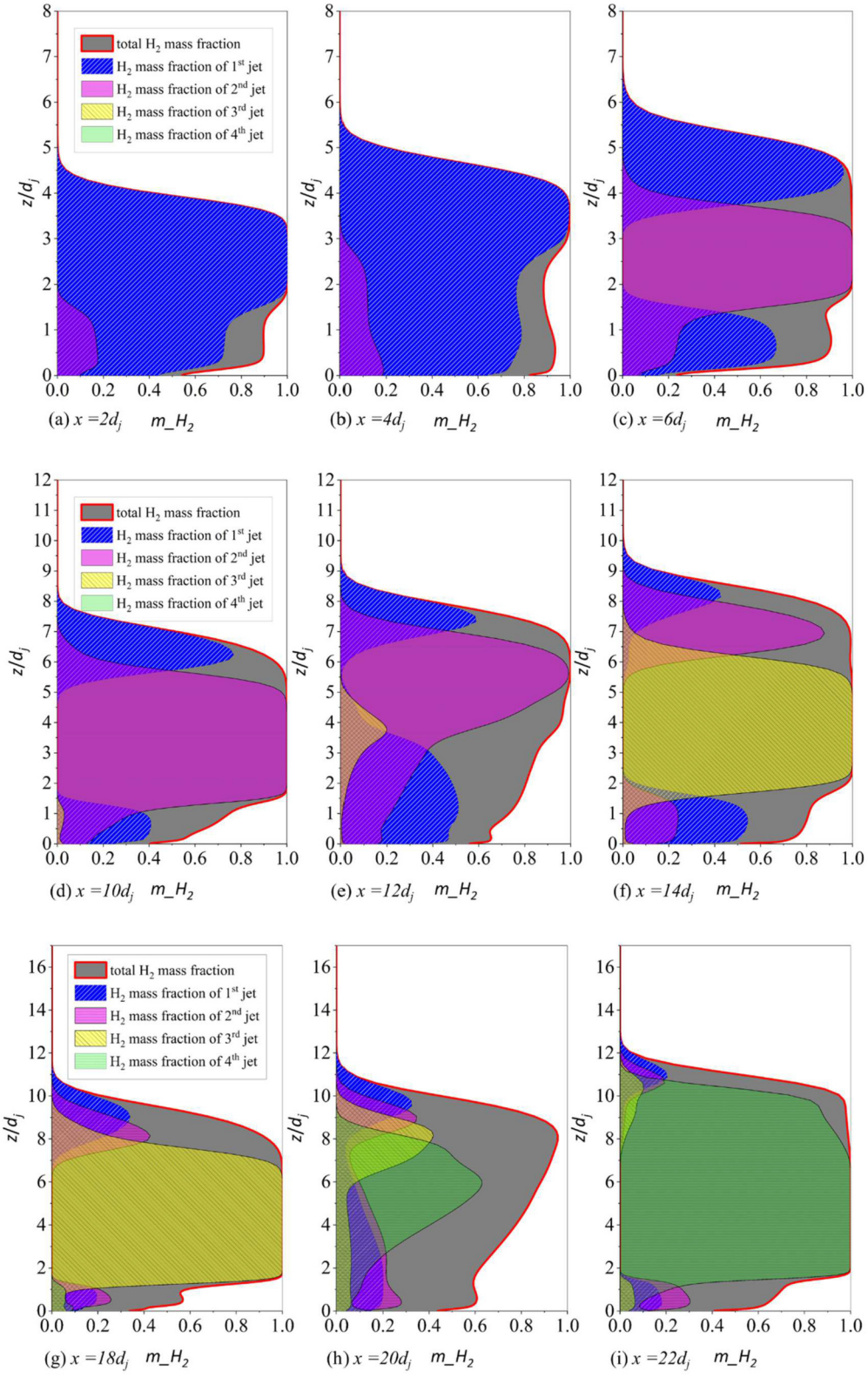

Fig. 18. Constitution of each jet in the tandem-arranged quadruple-jet case at different locations.

the second. However, as $x = 18d_j$ is far downstream, the contribution of the first jet in the near wall region is diminished and surpassed slightly by the second jet. This situation maintains till the last extracted line. Interestingly, from the outer region to the inner side, line $x = 20d_j$ goes through the jet plum originating from the first jet to the fourth in sequence. Except for the large contribution of the fourth jet, the hydrogen mass fraction from the first and second jets has nearly the same distribution along the lower half of the whole jet plum. Also, their contributions are greater than that of the third jet, though the third jet is closer to the third gap than the first and second jets.

In conclusion, injection from the first jet contributes most of the near wall hydrogen mass fraction except the far downstream line $x = 18d_j$ and mixes with all the other hydrogen from each jet. Additionally, injection from the third jet does not sufficiently spread into the upstream and downstream gap. Therefore, the upper-most jet could be replaced by an air jet to enhance the fuel-air mixing, and the third jet could be removed or relocated to a farther downstream location.

5. Conclusions

Sufficient fuel-air mixing is critical in the applications of ODEs. Premixed combustion, the main characteristic of detonation combustion, has two additional requirements compared with the fuel-air mixing in scramjet engines: pre-ignition prevention and sufficient fuel-air mixing in the hypersonic crossflow. To approach those goals, tandem-arranged equal-strength jets, viewed as the basic model of aero-ramp, were investigated numerically in this study. Three cases were conducted, including a single transverse jet and tandem-arranged double- and quadruple-jet, which ejected hydrogen transversely into a Mach 8 crossflow. The conclusions are as follows:

1. Jets downstream could not affect the Mach cell shape of the uppermost jet and the upstream bow shock curvature in the inter-gap ratio of $L/d_j = 8$. More jets in the downstream direction only slightly lifted the bow shock trajectories downstream.
2. Four recirculation regions appeared at the inter-region in tandem-arranged double-jet and quadruple-jet cases, including two strong recirculation regions and two secondary recirculation regions. Based on the streamline patterns, trailing vortex structures in the single transverse jet were replaced by two strong vortexes in the gap of the double-jet case, where the trailing vortex structure also widened. Vortex structures in the quadruple-jet case were not sufficiently developed.
3. High-temperature regions in the three cases were generated by the temperature rise brought by the separation shock and bow shock, which was also in the jet shear layer region and near the hydrogen stoichiometric equivalence ratio isoline ER=1 in the three cases, thus prone to pre-ignition.
4. By tracing the hydrogen ejected from each jet and comparing the mass fractions contributed by each jet in the quadruple-jet case, injection from the uppermost jet could cover the whole area behind the bow shock except the downstream Mach cell region, which also dominated the near wall hydrogen mass fraction construction within a long distance.

Based on the above conclusions, improvements could be made by replacing the first hydrogen jet in the quadruple-jet case with an air jet. In this way, the air ejected from the first jet could block the high-temperature region from the hydrogen, thus reducing the possibility of pre-ignition.

Though flow patterns were identified and improvements were made in tandem-arranged jets, a physical model is still needed to predict the basic parameter distributions in the flow field of multijet hypersonic crossflow interaction and direct the jet establishment, including jet position and strength. These tasks will be completed in our subsequent works.

Declaration of competing interest

The authors declare that they have no known competing financial interests or personal relationships that could have appeared to influence the work reported in this paper.

Data availability

The authors do not have permission to share data.

Acknowledgements

This work was supported by the National Natural Science Foundation of China (12132017, 11872066 and 11727901) and National Research and Development Program of China (2022YFB3207000).

References

[1] P. Wolanski, Detonative propulsion [J], Proc. Combust. Inst. 34 (2013) 125–158.
[2] H.H. Teng, P.F. Yang, Y.N. Zhang, et al., Flow and combustion mechanism of oblique detonation engines, Sci. Sin.-Phys. Mech. Astron. 50 (2020) 090008, https://doi.org/10.1360/SSPMA-2020-0144 (in Chinese).
[3] P. Yang, H. Teng, H.D. Ng, et al., A numerical study on the instability of oblique detonation waves with a two-step induction–reaction kinetic model [J], Proc. Combust. Inst. 37 (3) (2019) 3537–3544.
[4] Z. Zhang, C. Wen, W. Zhang, et al., Formation of stabilized oblique detonation waves in a combustor [J], Combust. Flame 223 (2021) 423–436.
[5] K. Wang, P. Yang, H. Teng, Steadiness of wave complex induced by oblique detonation wave reflection before an expansion corner [J], Aerosp. Sci. Technol. 112 (2021) 106592.
[6] Z. Zhang, Y. Liu, C. Wen, Mechanisms of the destabilized Mach reflection of inviscid oblique detonation waves before an expansion corner [J], J. Fluid Mech. 940 (2022) A29.
[7] J.P. Sislian, R. Dudebout, J. Schumacher, et al., Incomplete mixing and off-design effects on shock-induced combustion ramjet performance [J], J. Propuls. Power 16 (1) (2000) 41–48.
[8] Jiang Zonglin, Gaseous Detonation Physics and Its Universal Framework Theory, Science Press, Beijing, 2020 (in Chinese).
[9] Z. Zhang, K. Ma, W. Zhang, et al., Numerical investigation of a Mach 9 oblique detonation engine with fuel pre-injection [J], Aerosp. Sci. Technol. 105 (2020) 106054.
[10] G.P. Menees, H.G. Adelman, J-L. Cambier, et al., Wave combustors for trans-atmospheric vehicles [J], J. Propuls. Power 8 (3) (1992) 709–713.
[11] D. Papamoschou, A. Roshko, Observations of supersonic free shear layers [J], Sadhana 12 (1) (1988) 1–14.
[12] C. Zhang, R. Li, Z. Xi, et al., Effect of Mach number on the mode transition for supersonic cavity flows [J], Aerosp. Sci. Technol. 106 (2020) 106101.
[13] J. Chang, J. Zhang, W. Bao, et al., Research progress on strut-equipped supersonic combustors for scramjet application [J], Prog. Aerosp. Sci. 103 (2018) 1–30.
[14] S. Cox, R. Fuller, J.A. Schetz, et al., Vortical interactions generated by an injector array to enhance mixing in a supersonic flow [M], in: 32nd Aerospace Sciences Meeting and Exhibit, American Institute of Aeronautics and Astronautics, 1994.
[15] R.P. Fuller, P-K. Wu, A.S. Nejad, et al., Comparison of physical and aerodynamic ramps as fuel injectors in supersonic flow [J], J. Propuls. Power 14 (2) (1998) 135–145.

[16] R. Veraar, A. Mayer, J. Verreault, et al., Proof-of-principle experiment of a shock-induced combustion ramjet [M], in: 16th AIAA/DLR/DGLR International Space Planes and Hypersonic Systems and Technologies Conference, American Institute of Aeronautics and Astronautics, 2009.
[17] M. Gamba, M.G. Mungal, Ignition, flame structure and near-wall burning in transverse hydrogen jets in supersonic crossflow [J], J. Fluid Mech. 780 (2015) 226–273.
[18] S. Cox-Stouffer, M. Gruber, Effects of spanwise injection spacing on mixing characteristics of aerodynamic ramp injectors [M], in: 34th AIAA/ASME/SAE/ASEE Joint Propulsion Conference and Exhibit, American Institute of Aeronautics and Astronautics, 1998.
[19] S. Cox-Stouffer, M. Gruber, Further investigation of the effects of 'aerodynamic ramp' design upon mixing characteristics [M], in: 35th Joint Propulsion Conference and Exhibit, American Institute of Aeronautics and Astronautics, 1999.
[20] R. Fuller, P.K. Wu, A. Nejad, et al., Fuel-vortex interactions for enhanced mixing in supersonic flow [M], in: 32nd Joint Propulsion Conference and Exhibit, American Institute of Aeronautics and Astronautics, 1996.
[21] Q. Liu, D. Baccarella, T. Lee, Review of combustion stabilization for hypersonic airbreathing propulsion [J], Prog. Aerosp. Sci. 119 (2020) 100636.
[22] S-H. Lee, Characteristics of dual transverse injection in scramjet combustor, Part 1: mixing [J], J. Propuls. Power 22 (5) (2006) 1012–1019.
[23] S-H. Lee, Characteristics of dual transverse injection in scramjet combustor, Part 2: combustion [J], J. Propuls. Power 22 (5) (2006) 1020–1026.
[24] P. Li, Z. Wang, X-S. Bai, et al., Three-dimensional flow structures and droplet-gas mixing process of a liquid jet in supersonic crossflow [J], Aerosp. Sci. Technol. 90 (2019) 140–156.
[25] J. Huh, S. Lee, Numerical study on lateral jet interaction in supersonic crossflows [j], Aerosp. Sci. Technol. 80 (2018) 315–328.
[26] C-L. Qiao, H-Y. Xu, J. Li, et al., Parametric study on the sonic transverse jet in supersonic crossflow and analysis of the jet-crossflow interaction instability [J], Aerosp. Sci. Technol. 123 (2022) 107472.
[27] M. Zhao, Y. Bian, Q. Li, et al., Large eddy simulation of transverse single/double jet in supersonic crossflow [J], Aerosp. Sci. Technol. 89 (2019) 31–45.
[28] Z-B. Du, W. Huang, L. Yan, et al., Mixing augmentation mechanism induced by the dual injection concept in scramjet engines [J], Acta Astronaut. 156 (2019) 1–13.
[29] J.S. Smink, H.W.M. Hoeijmakers, C.H. Venner, Dual injection in supersonic crossflow: analysis jet shear layer from Schlieren images [J], AIAA J. 60 (11) (2022) 6277–6288.
[30] M.B. Gerdroodbary, Scramjets: Fuel Mixing and Injection Systems [M], Butterworth-Heinemann, 2020.
[31] F.R. Menter, Two-equation eddy-viscosity turbulence models for engineering applications [J], AIAA J. 32 (8) (1994) 1598–1605.
[32] H. Luo, J. Baum, R. Lohner, Extension of HLLC scheme for flows at all speeds, in: Proceedings of the 16th AIAA Computational Fluid Dynamics Conference [C], Orlando, Florida, F, American Institute of Aeronautics and Astronautics, 2003.
[33] S. Chakravarthy, O. Peroomian, B. Sekar, Some internal flow applications of a unified-grid CFD methodology, in: Proceedings of the 32nd Joint Propulsion Conference and Exhibit, F [C], American Institute of Aeronautics and Astronautics, 1996.
[34] J.R. Edwards, An implicit multigrid algorithm for computing hypersonic, chemically reacting viscous flows [J], J. Comput. Phys. 123 (1) (1996) 84–95.
[35] J.G. Santiago, J.C. Dutton, Velocity measurements of a jet injected into a supersonic crossflow [J], J. Propuls. Power 13 (2) (1997) 264–273.
[36] S. Kawai, S.K. Lele, Large-Eddy simulation of jet mixing in supersonic crossflows [J], AIAA J. 48 (9) (2010) 2063–2083.
[37] Z.A. Rana, B. Thornber, D. Drikakis, Transverse jet injection into a supersonic turbulent cross-flow [J], Phys. Fluids 23 (4) (2011) 046103.
[38] F. Génin, S. Menon, Dynamics of sonic jet injection into supersonic crossflow [J], J. Turbul. 11 (2010) N4.
[39] H.J. Lugt, The dilemma of defining a vortex [M], in: U. Müller, K.G. Roesner, B. Schmidt (Eds.), Recent Developments in Theoretical and Experimental Fluid Mechanics: Compressible and Incompressible Flows, Springer Berlin Heidelberg, Berlin, Heidelberg, 1979, pp. 309–321.
[40] C. Liu, Y. Gao, S. Tian, et al., Rortex—a new vortex vector definition and vorticity tensor and vector decompositions [J], Phys. Fluids 30 (3) (2018) 035103.
[41] Y. Gao, C. Liu, Rortex and comparison with eigenvalue-based vortex identification criteria [J], Phys. Fluids 30 (8) (2018) 085107.
[42] Y. Wang, Y. Gao, C. Liu, Letter: Galilean invariance of Rortex [J], Phys. Fluids 30 (11) (2018) 111701.
[43] C. Liu, Y-S. Gao, X-R. Dong, et al., Third generation of vortex identification methods: Omega and Liutex/Rortex based systems [J] 31 (2019) 205–223.
[44] P. Shrestha, C. Nottage, Y. Yu, et al., Stretching and shearing contamination analysis for Liutex and other vortex identification methods [J], Adv. Aerodyn. 3 (1) (2021) 8.
[45] X. Dong, Y. Gao, C. Liu, New normalized Rortex/vortex identification method [J], Phys. Fluids 31 (1) (2019) 011701.
[46] C. Liu, Y. Yan, P. Lu, Physics of turbulence generation and sustenance in a boundary layer [J], Comput. Fluids 102 (2014) 353–384.
[47] H. Li, D. Wang, H. Xu, Numerical simulation of turbulent thermal boundary layer and generation mechanisms of hairpin vortex [J], Aerosp. Sci. Technol. 98 (2020) 105680.
[48] N. Gui, L. Ge, P-X. Cheng, et al., Comparative assessment and analysis of Rortex vortex in swirling jets [J], J. Hydrodyn. 31 (3) (2019) 495–503.
[49] W-W. Zhao, J-H. Wang, D-C. Wan, Vortex identification methods in marine hydrodynamics [J], J. Hydrodyn. 32 (2) (2020) 286–295.